


Error-Divisible Two-Qubit Gates

David Rodríguez Pérez^{1,*}, Paul Varosy¹, Ziqian Li², Tanay Roy², Eliot Kapit¹ and David Schuster²

¹*Department of Physics, Colorado School of Mines, Golden, Colorado 80401, USA*

²*James Franck Institute, University of Chicago, Chicago, Illinois 60637, USA*

 (Received 15 January 2022; revised 9 January 2023; accepted 10 January 2023; published 15 February 2023)

We introduce a simple widely applicable formalism for designing “error-divisible” two-qubit gates: a quantum gate set where fractional rotations have proportionally reduced error compared to the full entangling gate. In current noisy intermediate-scale quantum (NISQ) algorithms, performance is largely constrained by error proliferation at high circuit depths, of which two-qubit gate error is generally the dominant contribution. Further, in many hardware implementations, arbitrary two-qubit rotations must be composed from multiple two-qubit stock gates, further increasing error. This work introduces a set of criteria, and example wave forms and protocols to satisfy them, using superconducting qubits with tunable couplers for constructing continuous gate sets with significantly reduced leakage and dynamic ZZ errors for small-angle rotations. If implemented at scale, NISQ-algorithm performance could be significantly improved by our error-divisible gate protocols.

DOI: [10.1103/PhysRevApplied.19.024043](https://doi.org/10.1103/PhysRevApplied.19.024043)

I. INTRODUCTION

Many advances in quantum hardware have focused on working toward fault-tolerant universal quantum computation [1–3]. However, the challenge of engineering a fully error-correcting logical qubit is a formidable one and advances in state coherence and gate errors need significant improvement before quantum computation reaches fault tolerance. Nevertheless, current qubit implementations have reached coherence and control levels such that they can perform NISQ algorithms [4] and may even be able to run tasks that surpass classical computers [5]. NISQ variational algorithms, such as the variational quantum eigensolver (VQE) and the quantum approximate optimization algorithm (QAOA) [6–8], have proven particularly useful in approximating the ground-state energy of difficult Hamiltonians. However, the performance of these algorithms depends on the circuit depth that can be achieved, which in turn depends on qubit coherence and gate error.

The inaccuracy of modern quantum algorithm implementations is dominated by two-qubit gate errors, as single-qubit gate errors are typically an order of magnitude smaller [9–14]. This is compounded by the traditional approach of implementing arbitrary two-qubit gates using a stock gate set, in which the large numbers of two-qubit rotations that may be required by a variational algorithm could be decomposed into at most three controlled-Z (CZ)

gates and additional single-qubit gates [15]. While this gate decomposition is crucial for digital error correcting codes [1], it proliferates gate error for NISQ algorithms needing a more diverse two-qubit gate set. To address this, research in implementing continuous sets of gates that perform arbitrary two-qubit rotations [16,17] has shown up to a 30% reduction in gate depth [18].

This work presents error-divisible gates that realize the smaller-angle two-qubit rotations that are prevalent in variational algorithms. The realization of smaller-angle rotations is done so at a corresponding smaller gate time—e.g., for full θ rotations at gate time t_g , $\theta/2$ rotations are done at $t_g/2$ time. This scheme directly reduces leakage errors and dynamic stray ZZ interactions. While it does not mitigate energy loss, dephasing, or static ZZ interactions, it can provide an opportunity to execute deeper circuits by indirectly reducing decoherence errors by virtue of having shorter gates.

A. Error divisibility

The basic idea for error divisibility is to implement a small two-qubit gate rotation without using multiple larger-rotation gates by instead proposing wave forms that are pulse shaped to perform fractional rotations at a corresponding fractional gate time. This is illustrated in Fig. 1(a), where a full two-qubit rotation θ_0 is achieved a gate time t_g and fractional rotations θ_0/n are run with corresponding gate times t_g/n . The full gate time t_g is chosen as small as possible so that the rotation θ_0 is executed at a chosen acceptable intrinsic error rate (not considering

*drodriguezperez@mines.edu

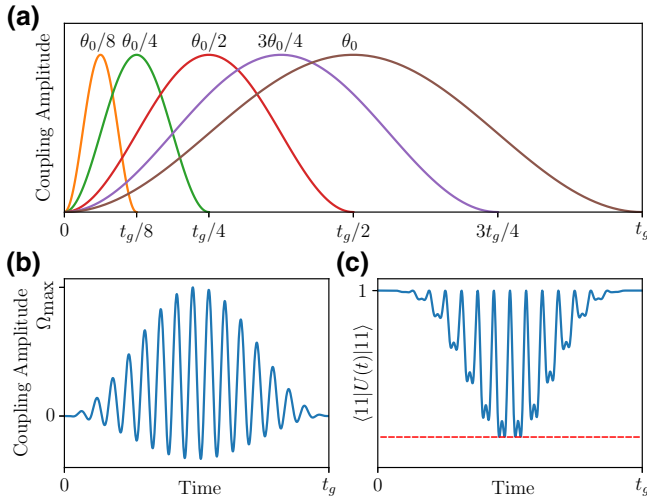


FIG. 1. An illustration of our proposed error-divisibility protocol. (a) Two-qubit rotation θ_0 at gate time t_g , along with fractional rotations θ_0/n at corresponding gate times t_g/n . Note that these wave forms are only meant to demonstrate the idea of error-divisible fractional rotations at fractional gate times and do not represent actual wave forms [amplitudes and frequencies—shown in (b)—can be different for each partial gate]. (b) An example gate-strength wave form for achieving error divisibility using a Gaussian gate envelope superimposed with a fast-oscillating counterterm. (c) The corresponding probability of gate $U(t)$ inducing transitions outside of $|11\rangle$ throughout the gate evolution in (b), where $U(t) = T \exp\left(-2\pi i \int_0^{t_g} \Omega(t) (|01\rangle\langle 10| + |10\rangle\langle 01|) dt\right)$ with coupling strength $\Omega(t)$ as in (b). An ideal exchange operation would preserve unity throughout the gate but accounting for nonlinear leakage states, we see off-resonant transitions outside of $|11\rangle$, creating these dips in (c), the maximum indicated by the red-dashed line. In typical operating regimes, the coupling strength in (b) is on the order of tens of megahertz, $t_g \approx 30$ ns, and the maximum dip from unity—which varies by the target rotation—can be $< 10^{-2}$ for appropriate parameter choices.

qubit decoherence). The fractional two-qubit gates implemented with the proposed protocol do not increase intrinsic qubit error significantly.

To address the difficulty in pulse-shaping gates of variable length for different target rotations, this work borrows ideas from Refs. [19,20], in which off-resonant energetics are used to suppress dispersive-shift effects. We propose simple wave forms that are superimposed Gaussian-like wave envelopes with fast-oscillating counterterms, as shown in Fig. 1(b). These wave forms do not require tuning of a large parameter space and significant errors are not introduced from small variations in the final wave form. Additionally, in Appendix B, we demonstrate the use of a single set of parameters for multiple fractional angle for a gate type, regurgitating the simplicity this scheme offers. The fast-oscillating counterterm serves to suppress intrinsic gate error throughout the duration of the

gate. Namely, the ones this work focuses on are leakage into higher-energy excited states and dynamic stray ZZ interactions that can create an effective partial controlled-phase (CPHASE) gate. These processes are the result of off-resonant mixing throughout the gate, which can be mitigated by additional off-resonant processes—realized as the fast-oscillating counterterms. This is illustrated in Fig. 1(c), where suppression of the gate error through the duration of the gate can be seen as a result of the oscillating wave form. The dashed red line indicates the maximum gate error, which can be reduced through minimal fine tuning of the small parameter space of the wave form.

While the work presented here completely ignores random qubit error such as amplitude dampening and dephasing, these are automatically addressed by the fact that this protocol shortens the gate time for each smaller rotation angle, allowing less time for decoherence. This provides an even bigger reduction in the error per gate than other continuous gate implementations [16,17], allowing for a greater circuit depth for NISQ algorithms without a significant increase in gate complexity.

II. PRINCIPLES OF IMPLEMENTATION

Consider two transmons with energies ω_1 and ω_2 with nonlinearity $-\delta$, coupled by the term $g(t) (a_1 + a_1^\dagger) (a_2 + a_2^\dagger)$. With appropriate choices of $g(t)$, we can resonantly drive a photon exchange between the two qubits. Choosing $g(t) = g_0 \Omega(t) \cos[2\pi(\omega_1 - \omega_2)t]$ gives us the rotating-frame Hamiltonian (Appendix A)

$$H = -\frac{\delta}{2} (a_1^\dagger a_1^\dagger a_1 a_1 + a_2^\dagger a_2^\dagger a_2 a_2) - \Omega(t) g_0 (a_1^\dagger a_2 + a_1 a_2^\dagger). \quad (1)$$

By going to second order in perturbation theory and eliminating the second excited energy state of the transmons, the qubit Hamiltonian becomes

$$H \simeq -\Omega(t) g_0 (\sigma_1^+ \sigma_2^- + \sigma_1^- \sigma_2^+) + \frac{\Omega(t)^2 g_0^2}{\delta} (1 + \sigma_1^z)(1 + \sigma_2^z), \quad (2)$$

where we can see an effective dispersive-shift term that applies a $\sigma_1^z \sigma_2^z$ term concurrently with the exchange Hamiltonian, $H = H_{\text{ex}} + H_{\text{ZZ}}$. To eliminate this dispersive shift, we let $\Omega(t)$ take on a shape like that of Fig. 1(b),

$$\Omega(t) = \Omega_0(t) [1 + \alpha \sin(2\pi f t)], \quad (3)$$

where $\Omega_0(t)$ is a slow evolving gate envelope, the fast-oscillating counterterm is determined by a frequency f , and α determines whether the wave form is positive valued—a condition required by some hardware implementations

[21]. Supposing that the slow evolving envelope in Eq. (3) is red detuned from the off-resonant transition causing phase accumulation, the fast-oscillating term adds a corresponding dispersive-shift blue-detuned term with opposite sign and can cancel it out. Examples of the engineering of these dispersive shifts from off-resonant processes are given in Ref. [22]. This is a similar approach to what has been discovered in Ref. [20], where an oscillatory offset proportional to the nonlinearity has been found to suppress population of the leakage states.

The examples presented here focus on exploring different wave envelopes $\Omega_0(t)$ for two different candidate gate systems— i SWAP(θ) = $\exp[i\theta/2(\sigma_1^+\sigma_2^- + \sigma_1^-\sigma_2^+)]$ and $XCX(\theta) = \exp[i\theta/4(1 + \sigma_1^x)(1 + \sigma_2^x)]$, where a full gate rotation θ_0 (like the illustration in Fig. 1) would be $\theta_0 = \pi$. The $XCX(\theta)$ gate set—the x -basis version of CPHASE(θ)—is chosen as it is easier to engineer than CPHASE. Also note that XCX reduces to single-qubit operations and one two-qubit XX operation, which along with i SWAP, becomes the focus of the following example wave forms.

We point out that the simulations done in this work are not complete open quantum system descriptions of two-qubit devices and a coupler device. We assume a rotating-frame Hamiltonian as in Eq. (2) and only concern ourselves with optimizing the gate pulse shape of the form

$$U(t) = Te^{-2\pi i \int_0^{t_g} \Omega(t)(V+P_1^2+P_2^2)dt}, \quad (4)$$

where V is the SWAP or XX interaction, defined as $V_{\text{SWAP}} = a_1^\dagger a_2 + a_1 a_2^\dagger$ or $V_{XX} = \tilde{\sigma}_1^x \tilde{\sigma}_2^x$, with $\{a^\dagger, a\}$ being the three-level creation and annihilation operators, $\tilde{\sigma}^x = a + a^\dagger$, and with $P_n^2 = |2_n\rangle\langle 2_n|$ as the projector onto the third state (leakage). Therefore, we concern ourselves here with optimizing the shape of $\Omega(t)$ in Eq. (4) to give the ideal i SWAP or XX operations.

A. Example wave forms

We propose some example wave forms with the characteristic fast-oscillating counterterm, as shown in Fig. 1(b). We focus on two different options for the slow evolving envelope $\Omega_0(t)$ in Eq. (3):

$$\Omega_0(t) = \frac{A}{2} \left[1 - \cos\left(2\pi \frac{t}{t_g}\right) \right], \text{ and} \quad (5a)$$

$$\Omega_0(t) = A \left[\tanh\left(\gamma \frac{t}{t_g}\right) - \tanh\left(\gamma \left[\frac{t}{t_g} - 1\right]\right) - \tanh\gamma \right]^2. \quad (5b)$$

For both Eqs. (5a) and (5b), the fast-oscillating part takes the form from Eq. (3), where we numerically tune the frequency f for different target rotations and choose $\alpha = 1$ for a positive-definite wave form and $\alpha = 2$ for wave

forms without such restrictions. A and γ are also numerically tuned for each target rotation, leaving only two parameters to tune for Eq. (5a) wave forms and three for Eq. (5b). These are shown in Fig. 2 for i SWAP and XX gates, using nonlinearity $\delta = 300$ MHz. Per the protocol laid out in Fig. 1, we first find a wave form for a full two-qubit rotation with a minimum gate time t_g while maintaining an acceptably low intrinsic error rate. We can then find wave forms for fractional rotations with corresponding fractional gate times, tuning the parameters A , γ , and f to maintain a low gate error. The results presented here do not consider decoherence and only account for leakage.

The error-rate results for these fractional gates are shown in Fig. 3. We can see that error divisibility is achieved for both i SWAP and XX gates down to 1/8th and 1/6th, respectively, using the profile in Eq. (5b)—this profile gives the best results. Considering that the target angle for a full XCX operation is half on an i SWAP, we expect this error-divisible scheme to break down faster for fractional XX operations, where small t_g starts to approach $1/\delta \approx 3$ ns. The limits of this scheme are evidenced by the noticeable increases in gate error down to 1/12 of a rotation, shown in Fig. 3, where we also point out a general higher gate error using positive-definite wave forms. We also note that intrinsic gate error can be further reduced using higher resolution in pulse shaping with a Fourier-series wave form to arbitrary precision. But this would require an arbitrary number of parameters to calibrate, making this option less desirable. The wave forms in Eq. (5) provide a simple parameter space to calibrate that matches experimental hardware. The complete set of criteria that we propose hopefully pave a way toward greater-depth circuits. The results and wave forms shown in Figs. 2 and 3 are obtained using unitary dynamics (ignoring energy loss and dephasing), and the parameters are found using differential-evolution methods [23].

III. HARDWARE IMPLEMENTATIONS

In the current state of superconducting hardware, advances in optimal control methods have mostly eliminated single-qubit gate errors [24–27]. However, multiple-qubit gate errors are still an order of magnitude greater than single-qubit gates [9–14], suffering from a combination of random qubit error during the gate, crosstalk [28–30], and calibration drift over time in systems using tunable architectures [31–33]. This error-divisible scheme intrinsically addresses random qubit error by reducing the duration of the gates in NISQ algorithms requiring smaller two-qubit rotations. This can be reliably done with our proposed scheme provided that there are no error-limiting steps. This means that gate protocols using tunable qubit energies [34,35], where coupling is done by bringing them into resonance with each other, cannot be considered for

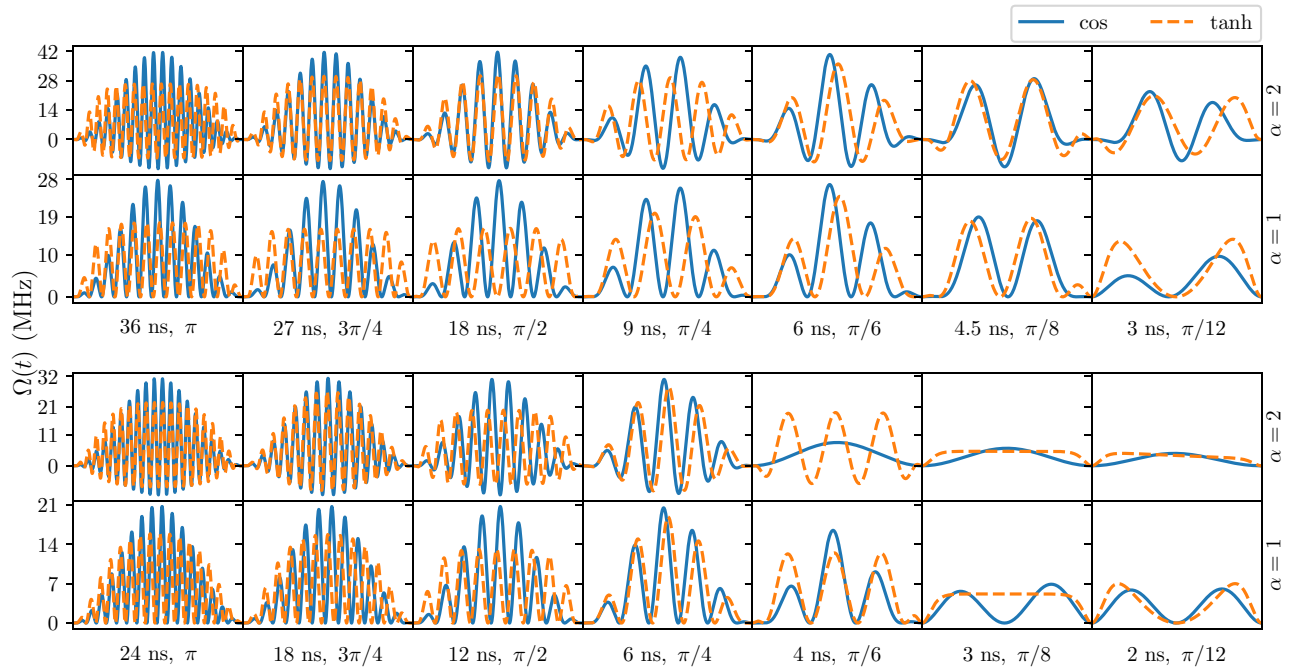


FIG. 2. Wave forms given by Eq. (5) for different rotations of *i*SWAP (top) and *XX* (bottom) gates. The wave forms for Eqs. (5a) and (5b) are labeled simply as “cos” and “tanh,” respectively, in the legend. The first row of both *i*SWAP and *XX* wave forms use $\alpha = 2$ in Eq. (3), while the bottom rows use $\alpha = 1$ to restrict the positivity of the wave forms. The full-rotation wave forms are on the far left and the subsequent plots reduce the target rotation and corresponding gate time by the fractional series $\{3/4, 1/2, 1/4, 1/6, 1/8, 1/12\}$.

this protocol due to the fixed amount of time necessary for tuning the qubit energies. The presence of fixed amounts of time also eliminates cross-resonance gates [36–39], where

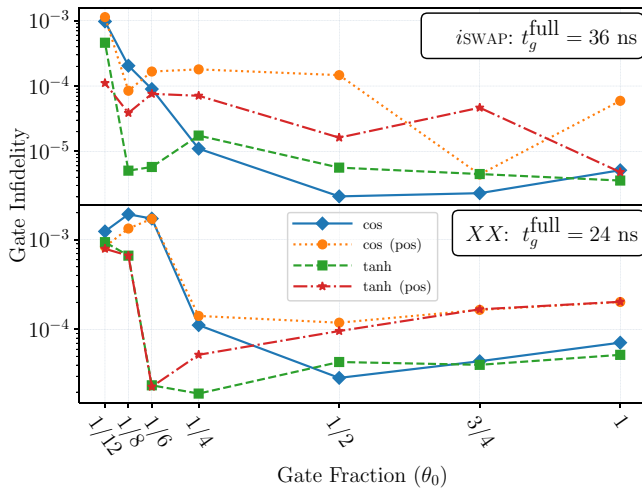


FIG. 3. Intrinsic gate-error results for fractional gate rotations for *i*SWAP (top, 36-ns gate for full π rotation) and *XX* (bottom, 24-ns gate for full π rotation) using both positive-definite (pos) and freely oscillating gate envelopes [see Eqs. (5a) (cos) and (5b) (tanh)]. For fractional *i*SWAP gates, we achieve a gate error $< 10^{-4}$ down to 1/8th of a gate using tanh envelopes and 1/6th for *XX* gates.

there is a minimum duration needed to suppress leakage in the process of driving qubits into higher excited energy states.

This leaves us with qubit architectures with fixed qubit energies [40–42], in which coupling is achieved by driving a coupler at the appropriate frequencies. Currently, the strongest coupler between transmons is able to generate a 100-MHz *i*SWAP gate [21,42], with the rate being limited by the qubit frequency and anharmonicity. Meanwhile, there is progress in pushing the transmon frequency to the millimeter-wave regime [43], which can be theoretically improved by an order of magnitude. In the future, this could allow an order of magnitude faster *i*SWAP gate in the millimeter-wave regime using a similar coupler design. Another limit in *i*SWAP and *XX* gate rates comes from the arbitrary wave-form generator (AWG) resolution. Current, commonly used commercial AWGs [44] have a 65 GSa/s sample rate, which can generate any wave form below 32.5 GHz. In Fig. 2, the required wave-form frequency is within the commercial AWG limit but higher than the current transmon-coupler limit. However, the error-divisible gate protocol is applicable to any frequency range. Therefore, by slowing down the gate, we can still generate wave forms for this scheme that are possible with current hardware capabilities, creating a path toward error divisibility for current transmon-based processors. While the wave forms presented in Fig. 2 are strictly difficult to implement with

current hardware, we explore the time scales to characterize the theoretical limitations of this protocol, as discussed in Sec. II A and demonstrated in Fig. 3.

The ability to realize this protocol with any system using a tunable coupler circuit allows for an easy generalization to qubits with large and small nonlinearities. Thus, while the analysis and simulations done in this work assume a transmon architecture, they are easily realizable for flux qubits [45–47] and fluxoniums [48,49].

IV. VQE EXAMPLE

To further motivate the use of the error-divisible protocol proposed in this work, we demonstrate the utility of running a variational algorithm with access to error-divisible gates. The example problem that we consider is an adiabatic evolution

$$H(t) = \left(1 - \frac{t}{T}\right) H_{\text{pin}} + \frac{t}{T} H_{\text{prob}}, \quad (6)$$

where T is the total run time, H_{pin} is a pinning Hamiltonian with an easily solvable solution, and H_{prob} is a harder problem Hamiltonian the ground state of which we are trying to determine by starting in the ground state of H_{pin} and adiabatically evolving $H(t)$. Approximating with a Trotter decomposition [50],

$$e^{-i dt(A+B)} = e^{-i dtA} e^{-i dtB} + O(dt^2), \quad (7)$$

we are able to implement the Hamiltonian as a collection of one- and two-qubit gates on hardware. Letting N be the number of Trotter layers, we set $dt = T/N$.

We choose to find the ground state of an antiferromagnetic Heisenberg model (AFM), letting the pinning and problem Hamiltonians in Eq. (6) be

$$H_{\text{pin}} = V \sum_{j \text{ even}} \sigma_j^z \quad (8a)$$

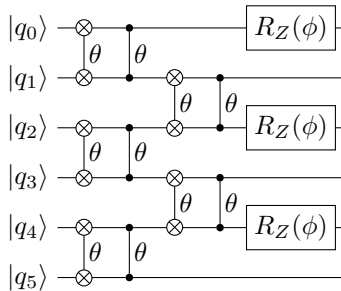


FIG. 4. The circuit diagram for a single layer of VQE implementing the Hamiltonian Eq. (8) using six qubits. The “ θ ” labels next to the i SWAP and CPHASE gates denote their partial rotations by angle θ .

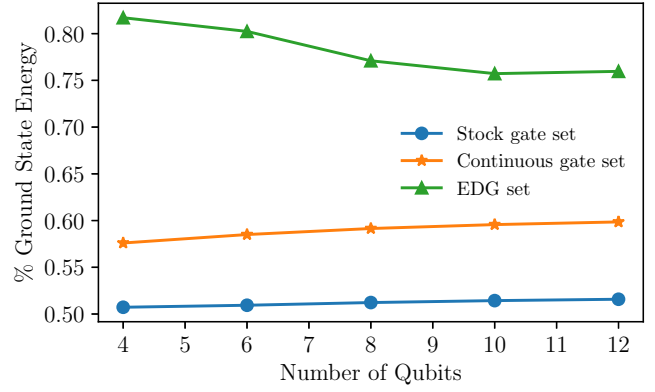


FIG. 5. Comparisons for the VQE fraction of the ground-state results using a stock gate set (blue square), continuous gates (orange star), and the proposed error-divisible gate scheme (green triangle).

$$H_{\text{prob}} = J \sum_{j=0}^{n_q-2} \left(\sigma_j^x \sigma_{j+1}^x + \sigma_j^y \sigma_{j+1}^y + \sigma_j^z \sigma_{j+1}^z \right), \quad (8b)$$

where n_q is the number of qubits and V and J are energy scales, which we set to $V = J = 1$ here. The circuit for Eq. (8) is shown in Fig. 4, where the Z rotations correspond to the pinning Hamiltonian given in Eq. (8a) and the i SWAP(θ) CPHASE(θ) sequence performs the problem Hamiltonian in Eq. (8b) using the approximation given in Eq. (7). T and N are optimized after every layer in Fig. 4, using a nonlinear optimization routine [51,52].

The primary error model considered here is a 1% depolarizing noise error rate for two-qubit gates and 0.1% for single-qubit gates. We compare the performance of this simulated variational algorithm using error-divisible gates, continuous gates [16,17], and a stock gate set. The results are shown in Fig. 5, with $\theta = 2J(t/N) dt$ and $\phi = 2V(1 - t/T) dt$. An implementation of Fig. 4 using a stock gate set would require two two-qubit gates and at least four single-qubit gates (Appendix C), giving an error rate of at least 2.4% per two-qubit operation in the VQE layer. With access to continuous gates, there would be no need for such decompositions and thus the two-qubit gate error rate is the 1% that we define. The use of error-divisible gates, implementing fractional gates with fractional gate times, results in a corresponding fractional error rate and is thus determined by N . These clear advantages are demonstrated in simulation as seen in Fig. 5, providing a clear example of the potential benefit in implementing error-divisible gates for near-term quantum computers.

V. CONCLUSIONS

We provide a set of criteria for implementing error-divisible two-qubit gates using currently available technology. We introduce the notion of fractional gates,

for which error divisibility provides a huge advantage for NISQ algorithms. At the heart of this criterion is the ability to generate a fast-oscillating wave form that can cancel dispersive-shift effects. To that end, we explore two sets of wave envelopes superimposed with fast-oscillating terms on two family of gates, i SWAP(θ) and XX (θ), and find error divisibility down to 1/6th and 1/8th of a full rotation, respectively. We then further motivate error-divisible gates by showcasing their potential advantage by simulating a variational algorithm for the adiabatic evolution of an AFM problem Hamiltonian.

ACKNOWLEDGMENTS

We would like to thank Eric Jones and Zhijie Tang for useful discussions. This work was supported by the National Science Foundation (NSF) (Grant No. PHY-1653820) and the Army Research Office (ARO) (Grant No. W911NF-18-1-0125). Simulations for the results in Sec. IV were obtained using the QuEST quantum simulator [53]. Both sets of results in Secs. II A and IV were obtained using the Wendian high-performance computer at the Colorado School of Mines.

APPENDIX A: HAMILTONIAN DERIVATION

We explicitly derive the rotating-frame Hamiltonian [Eq. (1)] for the two coupled qubits. Starting from the two coupled qubits with energies ω_1 and ω_2 and nonlinearity δ , the system is described by the Duffing-oscillator Hamiltonian in the energy basis as well as a coupling Hamiltonian,

$$H = \omega_1 \hat{n}_1 + \omega_2 \hat{n}_2 - \frac{\delta}{2} \left(a_1^\dagger a_1^\dagger a_1 a_1 + a_2^\dagger a_2^\dagger a_2 a_2 \right) + g(t) \left(a_1^\dagger + a_1 \right) \left(a_2^\dagger + a_2 \right), \quad (\text{A1})$$

where $\hat{n}_j = a_j^\dagger a_j$, $g(t) = g_0 A(t) \cos(2\pi(\omega_1 - \omega_2)t)$, and we let $\hbar = 1$. Recognizing this Hamiltonian with time-independent and time-dependent parts, $H(t) = H_0 + V(t)$, this obeys the Schrödinger equation $i\partial_t |\psi(t)\rangle = H(t) |\psi(t)\rangle$. We apply a unitary rotation transformation

$U_R(t)$ such that a new state can be defined:

$$|\phi(t)\rangle = U_R(t) |\psi(t)\rangle. \quad (\text{A2})$$

Looking at the time evolution of $|\phi(t)\rangle$,

$$\begin{aligned} i\partial_t |\phi(t)\rangle &= i\partial_t (U_R(t) |\psi(t)\rangle) \\ &= i\partial_t U_R(t) |\psi(t)\rangle + U_R(t) (i\partial_t |\psi(t)\rangle) \\ &= i\dot{U}_R(t) |\psi(t)\rangle + U_R(t) H(t) |\psi(t)\rangle \\ &= i\dot{U}_R(t) U_R^\dagger(t) |\phi(t)\rangle + U_R(t) H(t) U_R^\dagger(t) |\phi(t)\rangle, \end{aligned} \quad (\text{A3})$$

where we use Eq. (A2) to replace $|\psi(t)\rangle = U_R^\dagger(t) |\phi(t)\rangle$. From here, it is clear that the state $|\phi(t)\rangle$ also obeys the Schrödinger equation with a modified Hamiltonian

$$i\partial_t |\phi(t)\rangle = \left(i\dot{U}_R(t) U_R^\dagger(t) + U_R(t) H(t) U_R^\dagger(t) \right) |\phi(t)\rangle. \quad (\text{A4})$$

This is our rotating-frame Hamiltonian $i\partial_t |\phi(t)\rangle = H_R(t) |\phi(t)\rangle$. Separating the time-dependent part of the Hamiltonian given in Eq. (A1), we express $H_R(t)$ as

$$H_R(t) = i\dot{U}_R(t) U_R^\dagger(t) + U_R(t) H_0 U_R^\dagger(t) + U_R(t) V(t) U_R^\dagger(t), \quad (\text{A5})$$

allowing us to split this problem into solving three smaller parts. Letting $U_R(t) = e^{i(\omega_1 \hat{n}_1 + \omega_2 \hat{n}_2)t}$, we have

$$i\dot{U}_R(t) U_R^\dagger(t) = -(\omega_1 \hat{n}_1 + \omega_2 \hat{n}_2) \quad (\text{A6a})$$

$$\begin{aligned} U_R(t) H_0 U_R^\dagger(t) &= \omega_1 \hat{n}_1 + \omega_2 \hat{n}_2 \\ &\quad - \frac{\delta}{2} \left(a_1^\dagger a_1^\dagger a_1 a_1 + a_2^\dagger a_2^\dagger a_2 a_2 \right) \end{aligned} \quad (\text{A6b})$$

$$\begin{aligned} U_R(t) V(t) U_R^\dagger(t) &= -g(t) \left(a_1^\dagger e^{i\omega_1 t} + a_1 e^{-i\omega_1 t} \right) \\ &\quad \times \left(a_2^\dagger e^{i\omega_2 t} + a_2 e^{-i\omega_2 t} \right) \end{aligned} \quad (\text{A6c})$$

where we use the relations $a^\dagger e^{-i\omega t} = e^{i\omega t} a^\dagger$ and $a e^{-i\omega t} = e^{i\omega t} a$. Replacing $g(t)$ (ignoring 2π and

TABLE I. Parameters for the i SWAP wave-form results in Fig. 2 and the error rates in Fig. 3: the cosine profile [Eq. (5a)].

Fraction	t_g (ns)	Non-positive-definite ($\alpha = 2$)			Positive-definite ($\alpha = 1$)		
		A (MHz)	f (MHz)	Error (10^{-5})	A (MHz)	f (MHz)	Error (10^{-5})
1	36	13.91	-515.31	0.51	13.89	-377.61	5.93
3/4	27	13.91	-524.11	0.23	13.86	-374.14	0.44
1/2	18	13.87	-529.38	0.20	13.85	-410.17	14.67
1/4	9	13.84	-528.47	1.10	13.74	-528.06	17.98
1/5	6	13.77	-642.43	8.99	13.66	-644.62	16.67
1/8	4.5	13.04	-571.80	20.46	13.38	-548.56	8.46
1/12	3	10.25	-784.42	97.44	40.00	-183.81	113.59

TABLE II. Parameters for the *i*SWAP wave-form results in Fig. 2 and the error rates in Fig. 3: the tangent profile [Eq. (5b)].

Fraction	t_g (ns)	Non-positive-definite ($\alpha = 2$)				Positive-definite ($\alpha = 1$)			
		A (MHz)	f (MHz)	γ	Error (10^{-5})	A (MHz)	f (MHz)	γ	Error (10^{-5})
1	36	8.82	-523.28	9.37	0.36	8.83	-369.09	9.35	0.49
3/4	27	10.17	-525.38	6.32	0.45	8.06	-384.34	13.99	4.67
1/2	18	10.59	-525.40	5.74	0.56	8.16	-363.04	12.67	1.63
1/4	9	9.94	-591.50	6.40	1.74	10.23	-458.40	6.11	7.09
1/5	6	14.92	-576.66	3.62	0.58	14.85	-565.25	3.63	7.58
1/8	4.5	9.58	-593.94	9.06	0.51	9.50	-603.31	7.79	3.87
1/12	3	6.94	-684.12	15.00	4.60	40.00	-167.78	6.87	1.11

using $\cos[(\omega_1 - \omega_2)t]$ for the moment) and using Euler's formula, Eq. (A6c) becomes

$$\begin{aligned}
 U_R(t)V(t)U_R^\dagger(t) = & -\frac{g_0}{2}A(t)\left(a_1^\dagger a_2^\dagger e^{2i\omega_1 t} + a_1^\dagger a_2 e^{2i(\omega_1 - \omega_2)t}\right. \\
 & + a_1 a_2^\dagger e^{2i\omega_2 t} + a_1 a_2 e^{-2i(\omega_1 - \omega_2)t} \\
 & + a_1^\dagger a_2^\dagger e^{2i\omega_1 t} \\
 & + a_1^\dagger a_2 e^{2i\omega_2 t} + a_1 a_2^\dagger e^{-2i(\omega_1 - \omega_2)t} \\
 & \left. + a_1 a_2 e^{-2i\omega_1 t}\right). \quad (\text{A7})
 \end{aligned}$$

Making the rotating-wave approximation, we can discard all fast-oscillating terms and keep the slow-oscillating and stationary ones. Note that whether ω_1 and ω_2 are close together or far apart only changes the final result by a factor of 2 under the approximation, since the terms oscillating at $(\omega_1 - \omega_2)$ are the same as the stationary ones. Putting together Eqs. (A6) and (A7), our approximated rotating-frame Hamiltonian is

$$\begin{aligned}
 H_{RF} = & -\frac{\delta}{2}\left(a_1^\dagger a_1^\dagger a_1 a_1 + a_2^\dagger a_2^\dagger a_2 a_2\right) \\
 & - A(t)g_0\left(a_1^\dagger a_2 + a_1 a_2^\dagger\right). \quad (\text{A8})
 \end{aligned}$$

Letting $H_{RF} = H_0 + H_1$, with $H_0 = \delta/2\left(a_1^\dagger a_1^\dagger a_1 a_1 + a_2^\dagger a_2^\dagger a_2 a_2\right)$ and $H_1 = -A(t)g_0\left(a_1^\dagger a_2 + a_1 a_2^\dagger\right)$, we perturbatively find the effective Hamiltonian, treating $A(t)$ as

fixed for the moment. Ignoring states of higher energy than $|2\rangle$, the eigensystem for H_0 is given by

$$\begin{aligned}
 0\{|0_1 0_2\rangle, |0_1 1_2\rangle, |1_1 0_2\rangle, |1_1 1_2\rangle\}, \\
 -\delta\{|0_1 2_2\rangle, |2_1 0_2\rangle, |1_1 2_2\rangle, |2_1 1_2\rangle\}, -2\delta|2_1 2_2\rangle. \quad (\text{A9})
 \end{aligned}$$

Since the action of H_1 on any $|2\rangle$ state results in a $|3\rangle$ state, we ignore any corrections on those and focus on perturbative corrections for the $|0\rangle, |1\rangle$ subspace [0 eigenenergy states in Eq. (A9)]. Because these are degenerate, we diagonalize the perturbing Hamiltonian H_1 in this unperturbed eigenstate $|n^0\rangle$ subspace. Building out the $\langle n_i^0 | H_1 | n_j^0 \rangle$ matrix, we obtain

$$\begin{pmatrix} 0 & 0 & 0 & 0 \\ 0 & 0 & -A(t)g_0 & 0 \\ 0 & -A(t)g_0 & 0 & 0 \\ 0 & 0 & 0 & 0 \end{pmatrix}, \quad (\text{A10})$$

giving us the first-order corrections to the degenerate states

$$0(|0_1 0_2\rangle, |1_1 1_2\rangle), \pm \frac{A(t)g_0}{\sqrt{2}}(|1_1 0_2\rangle \mp |0_1 1_2\rangle). \quad (\text{A11})$$

The only state in this subspace with a nonzero second-order correction is $|1_1 1_2\rangle$, yielding $|0_1 2_2\rangle$ and $|2_1 0_2\rangle$ upon

 TABLE III. Parameters for the *XX* wave-form results in Fig. 2 and the error rates in Fig. 3: the cosine profile [Eq. (5a)].

Fraction	t_g (ns)	Non-positive-definite ($\alpha = 2$)			Positive-definite ($\alpha = 1$)		
		A (MHz)	f (MHz)	Error (10^{-5})	A (MHz)	f (MHz)	Error (10^{-5})
1	24	10.42	-854.11	7.11	10.42	-698.30	20.21
3/4	18	10.42	-861.22	4.42	10.41	-717.74	16.50
1/2	12	10.41	-850.74	2.88	10.39	-768.57	11.88
1/4	6	10.32	-955.75	11.16	10.31	-961.83	14.13
1/5	4	8.33	0.00	172.07	8.30	-923.54	171.03
1/8	3	6.27	0.00	191.99	40.00	-171.60	133.28
1/12	2	5.00	-9.06	123.77	40.00	-251.10	83.48

the action of H_1 , giving us

$$\frac{4A(t)^2 g_0^2}{\delta} |1_1 1_2\rangle. \quad (\text{A12})$$

Now eliminating second-excited energy states ($a^\dagger \rightarrow \sigma^+$, $a \rightarrow \sigma^-$), and up to second order in perturbation theory—combining Eqs. (A11) and (A12)—we obtain the effective Hamiltonian

$$H \simeq -A(t)g_0 (\sigma_1^+ \sigma_2^- + \sigma_1^- \sigma_2^+) + \frac{A(t)^2 g_0^2}{\delta} (1 + \sigma_1^z)(1 + \sigma_2^z). \quad (\text{A13})$$

This dispersive shift gives an effective CZ and partial *i*SWAP. To counter this, we can choose $A(t) = A_0(t)[1 + B \sin(2\pi ft)]$, where $A_0(t)$ is a slow evolving wave envelope. Given $f \gg g_0$, the leading exchange term in Eq. (A13) remains unaffected, while the oscillatory effects create off-resonant dispersive shifts that counter the effects of the $\sigma_1^z \sigma_2^z$ term.

APPENDIX B: SIMULATION DATA

In this appendix, we present simulated data for the wave-form results in Fig. 2 and the error rates in Fig. 3 (see Tables I–V). This set of data is obtained by numerically tuning the listed parameters for each individual two-qubit rotation. Note that for the really small gates (4 ns and smaller), this protocol starts to break down and thus we do

TABLE V. The data for the results plotted in Fig. 5, comparing the percentage of the ground-state energy that each type of gate set is able to produce.

Number of qubits	Stock	Continuous	Error-divisible
4	0.507243	0.575992	0.817031
6	0.509382	0.585032	0.802391
8	0.512273	0.59149	0.770956
10	0.514339	0.59568	0.757204
12	0.515807	0.598545	0.754664

not see a similar pattern in parameter choices determined by the numerical exploration.

We note that it would be convenient for a realization of this technique to use the same set of parameters for all partial rotations of a gate by tuning more parameters. For example, using device parameters for the current experimental realization—qubit nonlinearities $-0.16346 \times 2\pi$ GHz and $-0.254655 \times 2\pi$ GHz—and ignoring qubit energies in the rotating frame, if we modify Eq. (3) to $\Omega(t) = \Omega_0(t) [c + \alpha \sin(2\pi f t)]$ such that c and α can be arbitrarily tuned, using Eq. (5a) we can numerically find $\{A, f, \alpha, c\} = \{82.645 \text{ MHz}, 1.868 \text{ GHz}, 1.333, 0.336\}$ to obtain the gate errors $\{1.21, 0.67, 0.30, 0.49, 0.29, 7.43, 102.99\} \times 10^{-6}$, shown in Fig. 6.

APPENDIX C: REFERENCE IMPLEMENTATIONS

We use the following notation:

$$\begin{array}{c} \otimes \\ \text{---} \\ \otimes \end{array} = \boxed{i\text{SWAP}}, \quad \begin{array}{c} \otimes \\ \text{---} \\ \theta \\ \text{---} \\ \otimes \end{array} = \boxed{i\text{SWAP}(\theta)}, \quad \begin{array}{c} \otimes \\ \text{---} \\ \frac{\pi}{2} \\ \text{---} \\ \otimes \end{array} = \boxed{\sqrt{i\text{SWAP}}},$$

where $i\text{SWAP}(\theta) = \exp[i\theta/2 (\sigma_1^+ \sigma_2^- + \sigma_1^- \sigma_2^+)]$, with a full $i\text{SWAP} = i\text{SWAP}(\pi)$, and $\sqrt{i\text{SWAP}} = i\text{SWAP}(\pi/2)$. Using a stock native gate set—with a controlled-cnot (CNOT) as the base two-qubit gate, we can implement the two-qubit SWAP and *i*SWAP gates:

TABLE IV. Parameters for the *XX* wave-form results in Fig. 2 and the error rates in Fig. 3: the tangent profile [Eq. (5b)].

Fraction	t_g (ns)	Non-positive-definite ($\alpha = 2$)				Positive-definite ($\alpha = 1$)			
		A (MHz)	f (MHz)	γ	Error (10^{-5})	A (MHz)	f (MHz)	γ	Error (10^{-5})
1	24	7.66	-851.68	6.25	5.20	8.28	-715.89	5.38	20.31
3/4	18	10.08	-870.65	4.11	4.03	8.12	-752.41	5.56	16.74
1/2	12	6.62	-898.74	9.29	4.33	6.56	-801.57	9.52	9.59
1/4	6	12.52	-901.87	3.34	1.92	12.98	-909.24	3.24	5.21
1/5	4	6.34	-892.32	13.41	2.38	6.24	-903.65	13.65	2.29
1/8	3	5.18	0.00	15.00	66.43	5.18	0.00	15.00	66.43
1/12	2	5.00	-20.70	15.00	93.95	18.28	-250.01	8.09	79.21

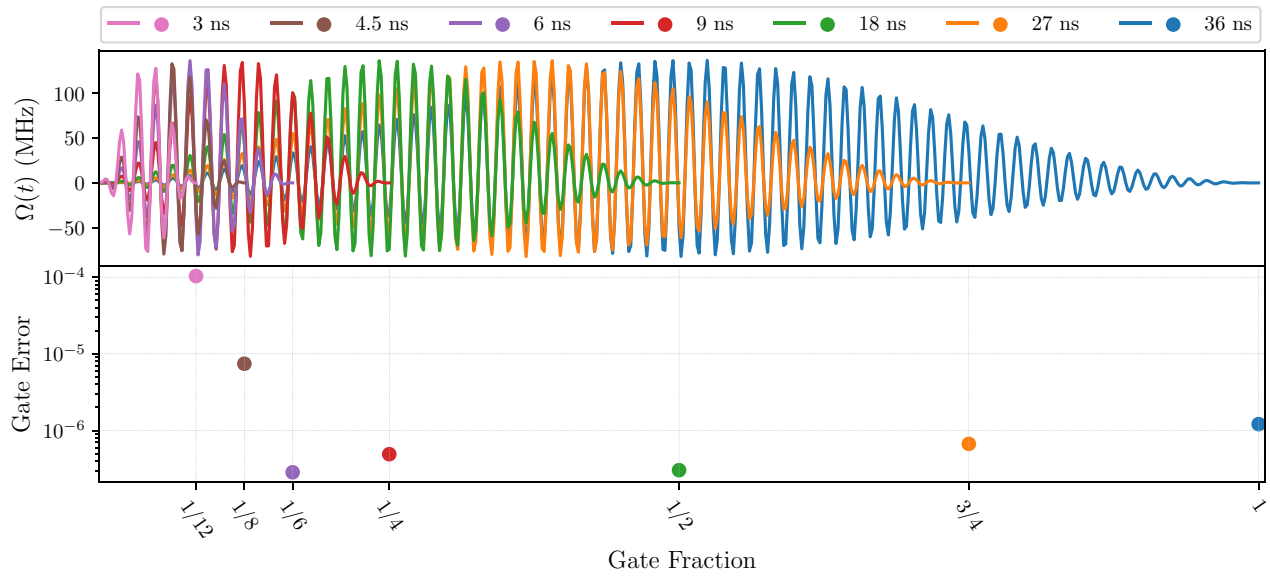


FIG. 6. Fractional gates using the same set of parameters, $\{A, f, \alpha, c\} = \{82.645 \text{ MHz}, 1.868 \text{ GHz}, 1.333, 0.336\}$ (top) to obtain the gate errors $\{1.21, 0.67, 0.30, 0.49, 0.29, 7.43, 102.99\} \times 10^{-6}$ (bottom).

$$\begin{array}{c} \times \\ \times \end{array} = \begin{array}{c} \oplus \\ \oplus \end{array} \begin{array}{c} \bullet \\ \bullet \end{array} \begin{array}{c} \oplus \\ \oplus \end{array}, \quad \begin{array}{c} \otimes \\ \otimes \end{array} = \begin{array}{c} S \\ S \end{array} \begin{array}{c} H \\ H \end{array} \begin{array}{c} \bullet \\ \bullet \end{array} \begin{array}{c} \oplus \\ \oplus \end{array} \begin{array}{c} H \\ H \end{array}.$$

With access to a broader set of native two-qubit gates, arbitrary two-qubit gates can be implemented more efficiently. For example, with access to a native $\sqrt{i\text{SWAP}}$, we can achieve the lowest-error implementation of SWAP that we are aware of, from Ref. [54]:

$$\begin{array}{c} \times \\ \times \end{array} = \begin{array}{c} \otimes \\ \otimes \end{array} \begin{array}{c} \pi/2 \\ \pi/2 \end{array} \begin{array}{c} R_X(-\pi/2) \\ R_X(-\pi/2) \end{array} \begin{array}{c} \otimes \\ \otimes \end{array} \begin{array}{c} \pi/2 \\ \pi/2 \end{array} \begin{array}{c} R_X(\pi/2) \\ R_X(\pi/2) \end{array} \begin{array}{c} R_Y(-\pi/2) \\ R_Y(-\pi/2) \end{array} \begin{array}{c} \otimes \\ \otimes \end{array} \begin{array}{c} \pi/2 \\ \pi/2 \end{array} \begin{array}{c} R_Y(\pi/2) \\ R_Y(\pi/2) \end{array}.$$

This explicitly demonstrates the benefit of having access to a native partial gate such as $\sqrt{i\text{SWAP}}$ for implementation of other two-qubit gates. More broadly, any arbitrary $i\text{SWAP}(\theta)$ rotation can be implemented using native $\sqrt{i\text{SWAP}}$ gates:

$$\begin{array}{c} \otimes \\ \otimes \end{array} \begin{array}{c} \theta \\ \theta \end{array} = \begin{array}{c} R_Z(\frac{3\pi}{4}) \\ R_Z(\frac{\pi}{4}) \end{array} \begin{array}{c} \otimes \\ \otimes \end{array} \begin{array}{c} \pi/2 \\ \pi/2 \end{array} \begin{array}{c} R_Z(\frac{\theta}{2} + \pi) \\ R_Z(-\frac{\theta}{2}) \end{array} \begin{array}{c} \otimes \\ \otimes \end{array} \begin{array}{c} \pi/2 \\ \pi/2 \end{array} \begin{array}{c} R_Z(\frac{\pi}{4}) \\ R_Z(-\frac{\pi}{4}) \end{array}.$$

This decomposition highlights the benefit of having access to a native set of arbitrary θ rotations that would allow the reduction of two-qubit gate error proliferation, as well as energy loss by virtue of spending less time on a single gate.

[1] A. G. Fowler, M. Mariantoni, J. M. Martinis, and A. N. Cleland, Surface codes: Towards practical large-scale quantum computation, *Phys. Rev. A* **86**, 032324 (2012).

[2] B. M. Terhal, Quantum error correction for quantum memories, *Rev. Mod. Phys.* **87**, 307 (2015).
 [3] R. Barends, *et al.*, Superconducting quantum circuits at the surface code threshold for fault tolerance, *Nature* **508**, 500 (2014).
 [4] J. Preskill, Quantum computing in the NISQ era and beyond, *Quantum* **2**, 79 (2018).
 [5] F. Arute, *et al.*, Quantum supremacy using a programmable superconducting processor, *Nature* **574**, 505 (2019).
 [6] M. P. Harrigan, *et al.*, Quantum approximate optimization of non-planar graph problems on a planar superconducting processor, *Nat. Phys.* **17**, 332 (2021).
 [7] A. Peruzzo, J. McClean, P. Shadbolt, M.-H. Yung, X.-Q. Zhou, P. J. Love, A. Aspuru-Guzik, and J. L. O’Brien, A variational eigenvalue solver on a photonic quantum processor, *Nat. Commun.* **5**, 4213 (2014).
 [8] J. R. McClean, J. Romero, R. Babbush, and A. Aspuru-Guzik, The theory of variational hybrid quantum-classical algorithms, *New J. Phys.* **18**, 023023 (2016).
 [9] J. Majer, J. M. Chow, J. M. Gambetta, J. Koch, B. R. Johnson, J. A. Schreier, L. Frunzio, D. I. Schuster, A. A. Houck, A. Wallraff, A. Blais, M. H. Devoret, S. M. Girvin, and

- R. J. Schoelkopf, Coupling superconducting qubits via a cavity bus, *Nature* **449**, 443 (2007).
- [10] F. Yan, P. Krantz, Y. Sung, M. Kjaergaard, D. L. Campbell, T. P. Orlando, S. Gustavsson, and W. D. Oliver, Tunable Coupling Scheme for Implementing High-Fidelity Two-Qubit Gates, *Phys. Rev. Appl.* **10**, 054062 (2018).
- [11] Y. Xu, J. Chu, J. Yuan, J. Qiu, Y. Zhou, L. Zhang, X. Tan, Y. Yu, S. Liu, J. Li, F. Yan, and D. Yu, High-Fidelity, High-Scalability Two-Qubit Gate Scheme for Superconducting Qubits, *Phys. Rev. Lett.* **125**, 240503 (2020).
- [12] P. Zhao, P. Xu, D. Lan, X. Tan, H. Yu, and Y. Yu, Switchable Next-Nearest-Neighbor Coupling for Controlled Two-Qubit Operations, *Phys. Rev. Appl.* **14**, 064016 (2020).
- [13] M. C. Collodo, J. Herrmann, N. Lacroix, C. K. Andersen, A. Remm, S. Lazar, J.-C. Besse, T. Walter, A. Wallraff, and C. Eichler, Implementation of Conditional Phase Gates Based on Tunable ZZ Interactions, *Phys. Rev. Lett.* **125**, 240502 (2020).
- [14] S. E. Rasmussen and N. T. Zinner, Simple implementation of high fidelity controlled-*i*SWAP gates and quantum circuit exponentiation of non-Hermitian gates, *Phys. Rev. Res.* **2**, 033097 (2020).
- [15] N. Khaneja and S. J. Glaser, Cartan decomposition of $SU(2^n)$ and control of spin systems, *Chem. Phys.* **267**, 11 (2001).
- [16] B. Foxen, *et al.*, Demonstrating a Continuous Set of Two-Qubit Gates for Near-Term Quantum Algorithms, *Phys. Rev. Lett.* **125**, 120504 (2020).
- [17] D. M. Abrams, N. Didier, B. R. Johnson, M. P. da Silva, and C. A. Ryan, Implementation of XY entangling gates with a single calibrated pulse, *Nat. Electron.* **3**, 744 (2020).
- [18] E. C. Peterson, G. E. Crooks, and R. S. Smith, Fixed-Depth Two-Qubit Circuits and the Monodromy Polytope, *Quantum* **4**, 247 (2020).
- [19] H. Xiong, Q. Ficheux, A. Somoroff, L. B. Nguyen, E. Dogan, D. Rosenstock, C. Wang, K. N. Nesterov, M. G. Vavilov, and V. E. Manucharyan, Arbitrary controlled-phase gate on fluxonium qubits using differential ac Stark shifts, *Phys. Rev. Res.* **4**, 023040 (2022).
- [20] D. R. Pérez and E. Kapit, Improved autonomous error correction using variable dissipation in small logical qubit architectures, *Quantum Sci. Technol.* **6**, 015006 (2020).
- [21] Y. Chen, *et al.*, Qubit Architecture with High Coherence and Fast Tunable Coupling, *Phys. Rev. Lett.* **113**, 220502 (2014).
- [22] E. Kapit, Error-Transparent Quantum Gates for Small Logical Qubit Architectures, *Phys. Rev. Lett.* **120**, 050503 (2018).
- [23] R. Feldt, robertfeldt/BlackBoxOptim.jl (2021).
- [24] F. Motzoi, J. M. Gambetta, P. Rebentrost, and F. K. Wilhelm, Simple Pulses for Elimination of Leakage in Weakly Nonlinear Qubits, *Phys. Rev. Lett.* **103**, 110501 (2009).
- [25] M. Möttönen, R. de Sousa, J. Zhang, and K. B. Whaley, High-fidelity one-qubit operations under random telegraph noise, *Phys. Rev. A* **73**, 022332 (2006).
- [26] S. Safaei, S. Montangero, F. Taddei, and R. Fazio, Optimized single-qubit gates for Josephson phase qubits, *Phys. Rev. B* **79**, 064524 (2009).
- [27] M. Steffen, J. M. Martinis, and I. L. Chuang, Accurate control of Josephson phase qubits, *Phys. Rev. B* **68**, 224518 (2003).
- [28] P. Mundada, G. Zhang, T. Hazard, and A. Houck, Suppression of Qubit Crosstalk in a Tunable Coupling Superconducting Circuit, *Phys. Rev. Appl.* **12**, 054023 (2019).
- [29] S. Sheldon, E. Magesan, J. M. Chow, and J. M. Gambetta, Procedure for systematically tuning up cross-talk in the cross-resonance gate, *Phys. Rev. A* **93**, 060302 (2016).
- [30] A. Winick, J. J. Wallman, and J. Emerson, Simulating and Mitigating Crosstalk, *Phys. Rev. Lett.* **126**, 230502 (2021).
- [31] S. Machnes, E. Assémat, D. Tannor, and F. K. Wilhelm, Tunable, Flexible, and Efficient Optimization of Control Pulses for Practical Qubits, *Phys. Rev. Lett.* **120**, 150401 (2018).
- [32] J. Stehlik, D. M. Zajac, D. L. Underwood, T. Phung, J. Blair, S. Carnevale, D. Klaus, G. A. Keefe, A. Carniol, M. Kumph, M. Steffen, and O. E. Dial, Tunable Coupling Architecture for Fixed-Frequency Transmons, *Phys. Rev. Lett.* **127**, 080505 (2021).
- [33] X. Dai, D. M. Tennant, R. Trappen, A. J. Martinez, D. Melanson, M. A. Yurtalan, Y. Tang, S. Novikov, J. A. Grover, S. M. Disseler, J. I. Basham, R. Das, D. K. Kim, A. J. Melville, B. M. Niedzielski, S. J. Weber, J. L. Yoder, D. A. Lidar, and A. Lupascu, Calibration of Flux Crosstalk in Large-Scale Flux-Tunable Superconducting Quantum Circuits, *PRX Quantum* **2**, 040313 (2021).
- [34] L. DiCarlo, J. M. Chow, J. M. Gambetta, L. S. Bishop, B. R. Johnson, D. I. Schuster, J. Majer, A. Blais, L. Frunzio, S. M. Girvin, and R. J. Schoelkopf, Demonstration of two-qubit algorithms with a superconducting quantum processor, *Nature* **460**, 240 (2009).
- [35] R. Barends, J. Kelly, A. Megrant, D. Sank, E. Jeffrey, Y. Chen, Y. Yin, B. Chiaro, J. Mutus, C. Neill, P. O'Malley, P. Roushan, J. Wenner, T. C. White, A. N. Cleland, and J. M. Martinis, Coherent Josephson Qubit Suitable for Scalable Quantum Integrated Circuits, *Phys. Rev. Lett.* **111**, 080502 (2013).
- [36] G. S. Paraoanu, Microwave-induced coupling of superconducting qubits, *Phys. Rev. B* **74**, 140504 (2006).
- [37] M. Malekakhlagh, E. Magesan, and D. C. McKay, First-principles analysis of cross-resonance gate operation, *Phys. Rev. A* **102**, 042605 (2020).
- [38] C. Rigetti and M. Devoret, Fully microwave-tunable universal gates in superconducting qubits with linear couplings and fixed transition frequencies, *Phys. Rev. B* **81**, 134507 (2010).
- [39] E. Magesan and J. M. Gambetta, Effective Hamiltonian models of the cross-resonance gate, *Phys. Rev. A* **101**, 052308 (2020).
- [40] D. C. McKay, S. Filipp, A. Mezzacapo, E. Magesan, J. M. Chow, and J. M. Gambetta, Universal Gate for Fixed-Frequency Qubits via a Tunable Bus, *Phys. Rev. Appl.* **6**, 064007 (2016).
- [41] S. A. Caldwell, *et al.*, Parametrically Activated Entangling Gates Using Transmon Qubits, *Phys. Rev. Appl.* **10**, 034050 (2018).
- [42] Y. Lu, S. Chakram, N. Leung, N. Earnest, R. Naik, Z. Huang, P. Groszkowski, E. Kapit, J. Koch, and D. I. Schuster, Universal Stabilization of a Parametrically Coupled Qubit, *Phys. Rev. Lett.* **119**, 150502 (2017).

- [43] F. Faramarzi, P. Day, J. Glasby, S. Sypkens, M. Colangelo, R. Chamberlin, M. Mirhosseini, K. Schmidt, K. K. Berggren, and P. Mauskopf, Initial Design of a W-Band Superconducting Kinetic Inductance Qubit, *IEEE Trans. Appl. Supercond.* **31**, 1 (2021).
- [44] *M8195A 65 GSa/s Arbitrary Waveform Generator*, Keysight Technologies, version 3.1.
- [45] T. P. Orlando, J. E. Mooij, L. Tian, C. H. van der Wal, L. S. Levitov, S. Lloyd, and J. J. Mazo, Superconducting persistent-current qubit, *Phys. Rev. B* **60**, 15398 (1999).
- [46] J. E. Mooij, T. P. Orlando, L. Levitov, L. Tian, C. H. van der Wal, and S. Lloyd, Josephson Persistent-Current Qubit, *Science* **285**, 1036 (1999).
- [47] L. B. Nguyen, Y.-H. Lin, A. Somoroff, R. Mencia, N. Grabon, and V. E. Manucharyan, High-Coherence Fluxonium Qubit, *Phys. Rev. X* **9**, 041041 (2019).
- [48] I. M. Pop, K. Geerlings, G. Catelani, R. J. Schoelkopf, L. I. Glazman, and M. H. Devoret, Coherent suppression of electromagnetic dissipation due to superconducting quasiparticles, *Nature* **508**, 369 (2014).
- [49] V. E. Manucharyan, J. Koch, L. I. Glazman, and M. H. Devoret, Fluxonium: Single Cooper-pair circuit free of charge offsets, *Science* **326**, 113 (2009).
- [50] N. Hatano and M. Suzuki, in *Quantum Annealing and Other Optimization Methods*, Vol. 679, edited by R. Beig, W. Beiglböck, W. Domcke, B.-G. Englert, U. Frisch, P. Hänggi, G. Hasinger, K. Hepp, W. Hillebrandt, D. Imboden, R. L. Jaffe, R. Lipowsky, H. v. Löhneysen, I. Ojima, D. Sornette, S. Theisen, W. Weise, J. Wess, J. Zittartz, A. Das, and B. K. Chakrabarti (Springer-Verlag, Berlin, 2005), p. 37.
- [51] P. Kaelo and M. M. Ali, Some variants of the controlled random search algorithm for global optimization, *J. Optim. Theory Appl.* **130**, 253 (2006).
- [52] S. G. Johnson, *stevengj/nlopt* (2021).
- [53] T. Jones, A. Brown, I. Bush, and S. C. Benjamin, QuEST and high performance simulation of quantum computers, *Sci. Rep.* **9**, 10736 (2019).
- [54] A. V. Lebedev, G. B. Lesovik, V. M. Vinokur, and G. Blatter, Extended quantum Maxwell demon acting over macroscopic distances, *Phys. Rev. B* **98**, 214502 (2018).